

RESEARCH

Open Access



# Research on mechanical characteristics and energy dissipation of traditional ramming technology

Qiangqiang Pei<sup>1,2,3,4</sup>, Xiaoying Liu<sup>1,3,4,5\*</sup>, Zhichun Hou<sup>2</sup>, Guojing Zhao<sup>1,3,4</sup>, Bo Zhang<sup>1,2,3,4</sup> and Qinglin Guo<sup>1,3,4</sup>

## Abstract

The ramming technique is a traditional method used to improve the compactness of soil with impact and vibration energy. Based on the measured data of ramming force transmission and dissipation, this study reveals the mechanism of energy transfer and dissipation of single-layer ramming as well as the law of variation with ramming quality, laying thickness, and ramming times. It also establishes the ramming model and empirical formula of ramming quality, laying thickness, and ramming times, introduces the ramming layer changes associated with the constitutive relationship (elastic to elastoplastic parts) as a function of ramming times, and determines the influence depth and horizontal range based on real-time data monitoring. It was found that as the mass of the rammer increases, the range of influence of the impact stress inside the earth also increases proportionally, and this effect is more pronounced vertically. However, the dissipation rate of energy in horizontal direction is much greater than in the vertical direction. The traditional stacked ramming technique of "chong hai wo, hang yin ding" can effectively eliminate the defects of horizontal reversal upwelling impact and unevenness of the ramming layer during the ramming process. The research results provide a theoretical basis for evaluating the quality of the traditional ramming technique.

**Keywords:** Earthen site, Ramming technique, Ramming mechanism, Energy dissipation

## Introduction

Since the primitive society, the development process of human society has experienced the emergence of caves, cave dwellings and ground buildings [1]. With the in-depth understanding of the earth's characteristics and the mastery of ramming technique, various geotechnical buildings have emerged in China [2–4]. In 2013, there were 4106 sites in the seventh batch of national key cultural relics protection units announced by the State Administration of Cultural Heritage, of which nearly 1000 were rammed earthen sites. With the development of society, this traditional ramming technique has been gradually replaced or completely eliminated due to the emergence of new materials, especially concrete [5,

6]. Moreover, these earthen sites are severely damaged by natural and human actions and need to be protected urgently. Therefore, the inheritance and application of traditional technique has become a key issue in sites conservation. Following the key scientific and technological project "Xia Shang Zhou chronology project" during the "Ninth Five-Year Plan" period, the "Chinese civilization exploration project", which combines multiple disciplines and studies of Chinese history and ancient culture, has become another major scientific research project supported by the state. So, the scientific cognition of traditional ramming technique of rammed earthen sites has become an widely studied academic issues in the field of cultural heritage conservation.

In ancient times, the traditional technique was handed down from generation to generation based on experience [7]. Over time, regional cultural differences, population migration and lack of written records gradually lead to

\*Correspondence: 1184009020@qq.com

<sup>1</sup> Dunhuang Academy, Mogao Grottoes, Dunhuang 736200, Gansu, China  
Full list of author information is available at the end of the article

the confusion and loss of rammed technique. In modern times, scholars represented by Liang Sicheng, Pan Guxi, and Liu Dake, have further explained, and speculated on the foundation, wall, building technology, and construction technology of the existing earthen sites through the book "Ying Zao Fa Shi". Zhang Hejun [8] and Wang Xingzhong [9] initially summarized the relationship between the types of traditional ramming tools and the development of ramming techniques. Jing Ai [10] et al. analyzed the origin, development process and construction technique of the Great Wall in different period through the literature. Xue Cheng [11] analyzed the ramming technique of Han Dynasty beacon towers from the history, method and process of ramming represented by Xinjiang Kizil Gaha Beacon Tower towers, and combined local construction techniques to form new technologies according to local conditions; Fu Jian [12] et al. deeply discussed earth moving tools, ramming tools, and ramming techniques. Xia Wei [13] and Li Bo [14] explored the reconstruction of visual expression of traditional earth materials combined with other materials through a series of rammed earth experiments and full scale experimental wall to let more people understand the rammed earth process and inherit the historical traditional technique. By analyzing the characteristics of traditional rammed earth technique. Zhou Tiegang [15] and Zhang Bo [16] et al. improved the traditional rammed materials, tools and processes through investigating traditional ramming technique and tools, explored the control methods of ramming technique and explained how to select ramming tools and technique. Pei Qiangqiang [17] et al. expounded the scientificity of traditional ramming technique and the influencing factors of ramming quality. Scholars have conducted a series of in-depth studies on the theoretical research, dynamic compaction effect and calculation model of modern dynamic consolidation, but there are few studies on the compaction mechanical characteristics and calculation model of ancient traditional compaction technology [18, 19]. Therefore, the

scientific explanation of the ramming mechanism and structural characteristics of the traditional ramming technique is the premise of further understanding and improving the traditional tamping technology.

In this study, the traditional ramming technique is simulated, and the foil micro pressure box is used to measure the ramming stress and energy dissipation under the conditions of different paving thickness, rammer and ramming times. The dissipation mechanism and law of ramming energy are expounded by using dynamics and elastic-plastic theory. Through the finite element analysis software, the mathematical models of ramming stress in the above three cases are fitted, and the stress characteristics and stress influence range of different rammers are summarized. The research results have a clear scientific understanding of the traditional ramming technique. This study provides a reliable theoretical basis for evaluating the quality of traditional ramming technique, and also provides technical parameters for the tradition, excavation, application and final conservation of earth sites. At the same time, it can promote the scientific and systematic development of earth site conservation discipline.

## Test materials and methods

### Test material

The site soil is the site soil of Western Xia Imperial Tombs in Yinchuan City, Ningxia Province, China, and the test soil is taken from the Loess near the site of Western Xia Imperial Tombs. The mineral composition and particle size distribution of the soil samples are listed in Tables 1 and 2 (weight percentages). The basic physical and mechanical properties of the soil were obtained according to basic geotechnical tests and triaxial tests, as detailed in Table 3.

### Test apparatus

#### Ramming mold

The traditional ramming technology mold is classified into two types: plate and rafter (Fig. 1). The test in this

**Table 1** X-ray diffraction (XRD) mineral composition analysis (unit: %)

Sample name	Quartz	Calcite	Dolomite	Feldspar	Illite	Chlorite
Site soil	33	19	17	9	12	10
Test soil	30	25	7	9	21	7

**Table 2** Particle size distribution (unit: %)

Particle size distribution (mm)	>20	10–20	5–10	2–5	1–2	0.5–1	0.25–0.5	0.075–0.25	0.005–0.075	<0.005
Test soil	0.15	1.71	4.24	5.68	0.27	2.89	1.77	28.63	50.16	4.51

study adopts the rafter ramming method (known as the frame rod ramming method) commonly used in Northwest China. Regarding the test wall, its length is 3.40 m, width is 1.0 m, rafter length is 3.50 m, and diameter is in the range 12–18 cm. There are five rafter pieces on each test wall. The side plate is spliced with five wood plates (thicknesses of 3 cm), and the plates on both the sides are triangular. The entire side plate is spliced to form a trapezoid with a width of 1.0 m at the bottom,

width of 0.6 m at the top, and height of 2.40 m. The buried depth of the root of the six columns should not be less than 30 cm, and the bottom, middle, and top (both sides) should be tied by bolts with  $\Phi 18$  steel bars on both the sides. The diameter of the column should be in the range of 15–20 cm, and the length should be 3 m. A wooden wedge was used between the rafter wedge and column to form a closed mold.

**Table 3** Basic physical and mechanical properties of remodeling samples

Types	Natural moisture content(%)	Optimum moisture content (%)	Specific gravity	Boundary moisture test			Mechanical properties	
				Liquid limit (%)	Plastic limit (%)	Plasticity index	Cohesion (kPa)	Internal friction angle (°)
Test soil	1.8	13.3	2.73	29.70	19.30	10.40	25.142	30.23

Medium sand (0.25–0.5 mm), fine sand (0.075–0.25 mm), fine particle group (<0.075 mm)



**Fig. 1** Ramming mold: (a) front view of ramming mould; (b) side view of ramming mould

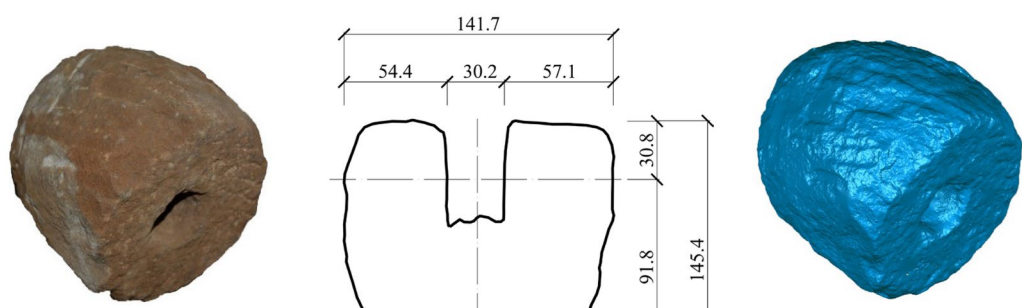


**Fig. 2** Unearth pestle and its size from No. 3 tomb in the Western Xia Imperial Tombs and three-dimensional scan

### Rammer

Traditional ramming tools are usually made of stone or wood. The analysis of the stone pestle unearthed from the No. 3 Mausoleum (Western Xia Imperial Tombs) shows that its mass is 3.34 kg, diameter is 14.17 cm, height is 14.54 cm, volume is 1632.51 cm<sup>3</sup>, density is 2.047 g/cm<sup>3</sup>, and material is sandstone (Fig. 2). According to its curvature and diameter, five types of rammers with different specifications were constructed. According to the diameter from small to large, it was numbered as hammer No. 1 to No. 5, and its diameter and weight are presented in Table 4 and Fig. 3.

### Foil-type miniature pressure box

The foil micro pressure box is composed of a high-quality alloy material, a round film gum base full bridge foil strain gauge, and a special sealing process. With the use of the pressure box of the film conversion type, the foil strain gauge is pasted on the deformed film, and the external force of the pressure box is determined by measuring the strain value of the foil strain gauge.

### Ramming process

#### Preparations before the test

The ramming method adopts the traditional ramming process. Before ramming, the mold is supported, and the soil is laid after ensuring that the mold is firmly supported. The thickness of the soil is subject to the experimental plan (error  $\leq 0.5$  cm). In order to ensure the quality of rammed soil, after each experimental virtual soil is laid, random samples are taken to test its moisture content to ensure that the moisture content of the rammed soil is within the error range (13.3  $\pm$  0.5%) [20]. If



**Fig. 3** Photograph showing five types of rammers

the moisture content test results deviate from the allowable range, reorganize the group of experiments (Fig. 4).

#### 'Na xu pan cai' (step-on)

'Na xu pan cai' refers to the process of stepping on loose soil with one's feet [17]. After the loose soil is laid, use the rammer to ram it with one's feet (Fig. 5a). The whole step-on experiment was done by one person. The purpose of step-on was to reduce the resistance of the rammer when it was put into the soil and then lift it up during the first ramming, also to prevent the loose soil from splashing.

#### Ramming method

The ramming technique [17] is rammed step by step according to the traditional ramming technique of 'chong hai wo, hang yin ding' (Fig. 5b), that is, the first time is 'chong hai wo' (Fig. 5c), the adjacent rammer nests are close together, and the second time is 'hang yin ding' (Fig. 5d). Each area is rammed row by row according to the method of 'chong hai wo, hang yin ding', and the ramming sequence of each row is from east to west. In the process of ramming, the lifting height of the rammer should be kept as consistent as possible, and the force should be even, and record the number of ramming times in each area (Fig. 5).

**Table 4** Ramming tests

Rammer number	No. 1	No. 2	No. 3	No. 4	No. 5
Diameter (mm)	100	120	140	160	180
Mass (kg)	3.32	4.03	5.50	9.97	15.02
Raised rammer height (m)	0.25	0.25	0.22	0.21	0.2

**Table 5** Maximum stress values corresponding to different rammers and soil-laying thicknesses (experiments)

Soil thickness	No. 1 rammer (kPa)	No. 2 rammer (kPa)	No. 3 rammer (kPa)	No. 4 rammer (kPa)	No. 5 rammer (kPa)
20 cm	298	279.5	362	656.8	530
16 cm	383	357.2	520	434	727
12 cm	471	493.4	506.7	576.4	718
8 cm	1347	1251.8	1829.7	2753.8	1858.6



(a) Support mold



(b) Lay the soil and level



(c) Measuring soil thickness



(d) Sampling

**Fig. 4** Prep work. **a** Support mold, **b** Lay the soil and level, **c** Measuring soil thickness, **d** Sampling

### Test method

According to the size of the five rammers, they are divided into five areas. From left to right, the selected different rammers correspond to No. 1, No. 2, No. 3, No. 4, and No. 5 (Fig. 3). The foundation is rammed many times by dynamic compaction, and its settlement deformation can be ignored. The ramming stress of different times of ramming in different areas was tested when the single-layer soil thickness was 8 cm, 12 cm, 16 cm, 20 cm and multi-layer ramming respectively. Photograph showing five types of compaction is shown in Fig. 6.

The specific test procedures are as follows:

- (1) Pretest inspection checks whether the pressure box and its leads are in good condition. This is followed by the connection of the collector, placement on a horizontal position, and by testing whether its value is stable after preheating for 30 min (the value fluctuation is less than its measurement accuracy).
- (2) Sand coating. Mark the location where the pressure box is placed and lay standard sand with a

thickness in the range of 2–4 mm at the determined location to eliminate local stress errors caused by nonuniform medium. The area of covering sand should not be less than three times the surface area of the pressure box.

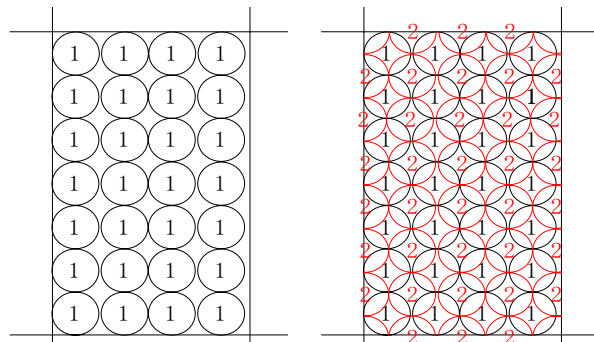
(3) Place the pressure box (Fig. 7). Place the earth pressure box on the standard sand (Fig. 8a), lightly press both sides of the earth pressure box (Fig. 8b), compact and fix the pressure box and the lead wire with earth material to prevent the pressure from moving and overturning owing to the effects of the external force (Fig. 8c), lead the wire out from the foundation, and record the earth pressure box and lead wire.

(4) Lay soil. Pave the soil according to the designed thickness (Fig. 8d) first around the lead wire and pressure box, and gradually expand to other areas to ensure the stability and lack of displacement of the pressure box during the soil-paving process.

(5) Link the collector. When the soil-laying process is completed, the lead of the pressure box is con-



(a) 'Na xu pan cai' (step-on)



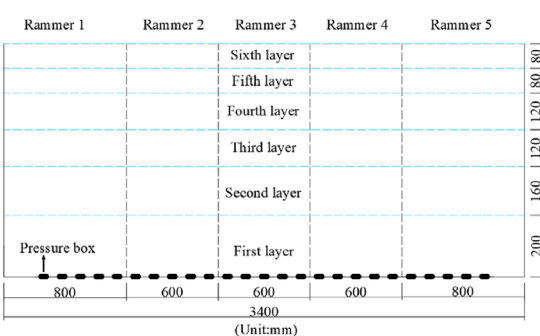
(b) Schematic diagram of ramming



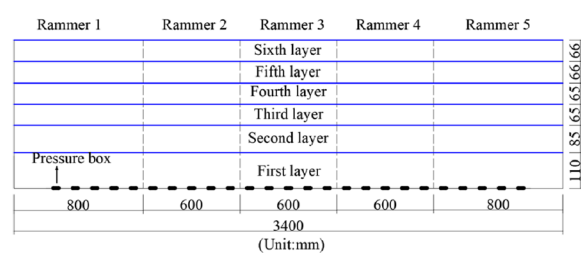
(c) 'chong hai wo'



(d) 'hang yin ding'

**Fig. 5** Ramming method. **a** 'Na xu pan cai' (step-on). **b** Schematic diagram of ramming. **c** 'chong hai wo'. **d** 'hang yin ding'

(a) Loose soil thickness



(b) Thickness of soil after ramming(dense soil thickness)

**Fig. 6** Multi-layer ramming section drawing. **a** Loose soil thickness, **b** Thickness of soil after ramming (dense soil thickness)

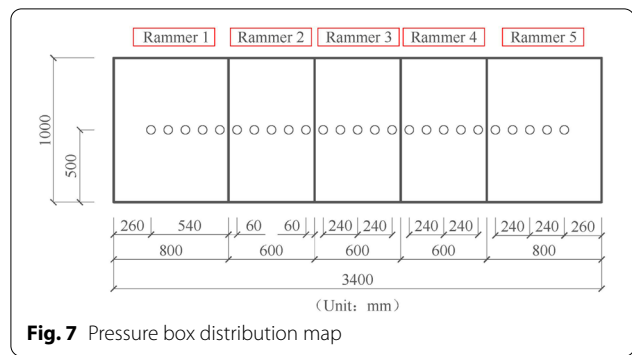


**Fig. 7** Pressure box distribution map

nected with the lead of the dynamic signal test and analysis system in sequence with the full bridge method. After checking, activate the test software, set the parameters, preheat for 30 min, reset the balance, and initiate data collection.

(6) Data collection. The wall should be rammed according to the test plan, and the stress of the pressure box should be tested simultaneously. The sampling frequency should be greater than 1 kHz and should not be stopped in the middle until the test is completed.

## Ramming model and description

### Motion model of test rammer

The idea of establishing a dynamic model of a ramming test comes from dynamic compaction [21, 22]. Dynamic compaction involves the use of an impact dynamic load to reduce the pore volume in the soil and render the soil more compact to improve its strength and maintain the stability of its structure. The ramming energy mainly propagates in the form of a vibration wave in the virtual soil, and the other part is consumed by frictional heat, sound waves propagating in the air, and air-flow resistance at the bottom of the rammer. Not all of the vibration wave energy plays a reinforcing role. Therefore, it is necessary to analyze the effective proportion of the ramming energy that can be expressed by the efficiency coefficient  $\eta$ . The value of  $\eta$  is generally in the range of 0.5–0.9 [23–27].

According to the motion mode of the rammer (Fig. 9), the formula used for the calculation of the impact force is derived from the momentum theorem: when an object with a gravity force equal to  $mg$  (where  $m$  is the mass, and  $g$  is the acceleration of gravity) falls freely from a height  $h$ , the impact force on the ground is  $F$ , and the initial grounding speed of the object is  $v_I$ . After contact with



**(a)** Cover with standard sand



**(b)** Place the pressure box

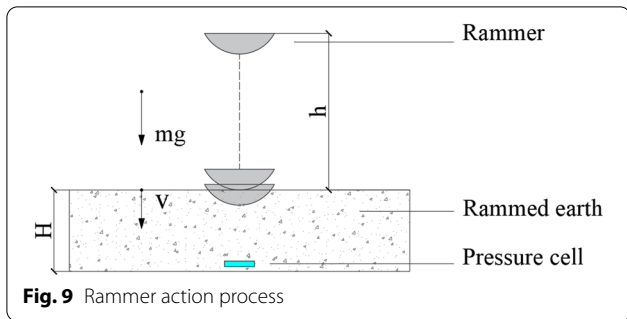


**(c)** Pressing line



**(d)** Cover soil

**Fig. 8** Ramming test flow chart. **a** Cover with standard sand. **b** Place the pressure box. **c** Pressing line. **d** Cover soil

**Fig. 9** Rammer action process

the ground, the speed changes to  $v_2$  (generally for the rammer,  $v_2$  is zero). According to the momentum theorem, the impulse of an object to the ground ( $F - mg$ )  $\Delta t$  is equal to the change in the momentum of the object  $mv_2 - mv_1$ ,

$$(F - mg)\Delta t = -(mv_2 - mv_1) \quad (1)$$

Therefore,  $v_1 = \sqrt{2gh}$ ,  $v_2 = 0$

$$F = mg \left( 1 + \sqrt{\frac{2h}{g} \frac{1}{\Delta t}} \right) = mgh \left( \frac{1}{h} + \sqrt{\frac{2}{gh} \frac{1}{\Delta t}} \right) \quad (2)$$

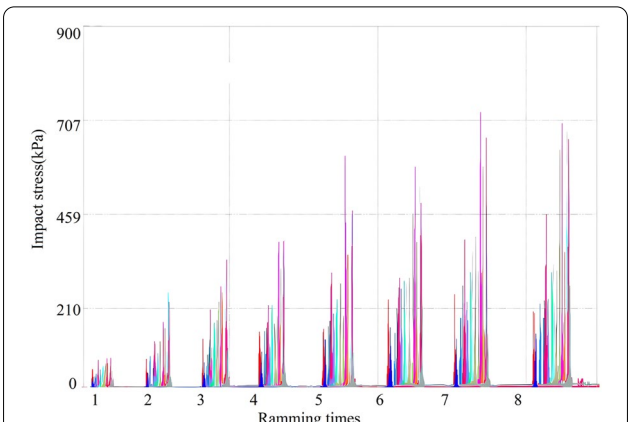
$$\sigma = \frac{F}{S} \quad (3)$$

where  $S$  is the contact area between the bottom of the rammer and the soil, and  $\sigma$  is the Raman pressure at the bottom part.

It should be noted that the impact force of the rammer on the ground is  $F - mg$ , however,  $F$  is much larger than  $mg$ . We usually call  $F$  the impact force. From Eq. (2), it can be concluded that  $F$  is directly proportional to the single-click energy of the rammer ( $mgh$ ).

#### Stress characteristics of different tamping times

Figure 10 shows the change in impact stress on the earth pressure box recorded by the dynamic testing and analysis system when different rammers tamp the covering soil (with a thickness of 20 cm) eight times. To reduce human factors and provide a reference for the analysis of the ramming results of other layers, the ramming process of this layer (repeated eight times) was completed by the same person. As it can be observed from the figure, the impact stress measured by the 25 pressure boxes was relatively small during the first ramming, and with the increase in ramming times, the impact force measured by the corresponding pressure boxes also increased gradually. According to the increase rate, the process can be divided into two stages: the increase in speed is fast

**Fig. 10** Recorder image of covering soil at a depth of 20 cm at different ramming times (experiments)

from the first to the sixth ramming time, and the increase in speed is slow from the sixth to the eighth ramming time. This is because before ramming, the earth is loose, the ramming energy is seriously lost in the transmission process. With the increasing of ramming times, the earth compactness increases, and the loss of ramming energy decreases, and the energy transmitted to the pressure box increase gradually. The earth density increases rapidly after 1–6 times, which is the direct reason for the rapid increase rate of impact stress. It is difficult to increase the earth density during 6–8 times of ramming, and the impact stress also slow down.

Figure 11 shows the rammed stress diagrams corresponding to five types of rammers, different soil thicknesses, and different ramming times. It can be observed that the impact force on the pressure box decreases gradually as a function of the thickness of the covering soil, and the impact stress increases with the increasing of rammer mass and ramming times. Generally, the ramming stress growth rate increases from the first to the sixth repetition and slows down after the sixth repetition. This shows that use of one to six compaction times is most effective. Use of more than six times, makes part of the compaction force transmission become far-reaching. Accordingly, the effectiveness of the work on the compaction layer is weakened.

As it can be observed from Fig. 11 and Table 5, the different paving soil thicknesses have different requirements based on the rammer weight. The overall trend indicates that as the thickness increases, the rammer weight needs to be increased to meet the requirement for improved ramming stress transmission. For example, when the paving thickness is only 8 cm, the rammers No. 1 to No. 5 can transmit ramming energy very well. When the paving thicknesses are 12 cm, 16 cm,

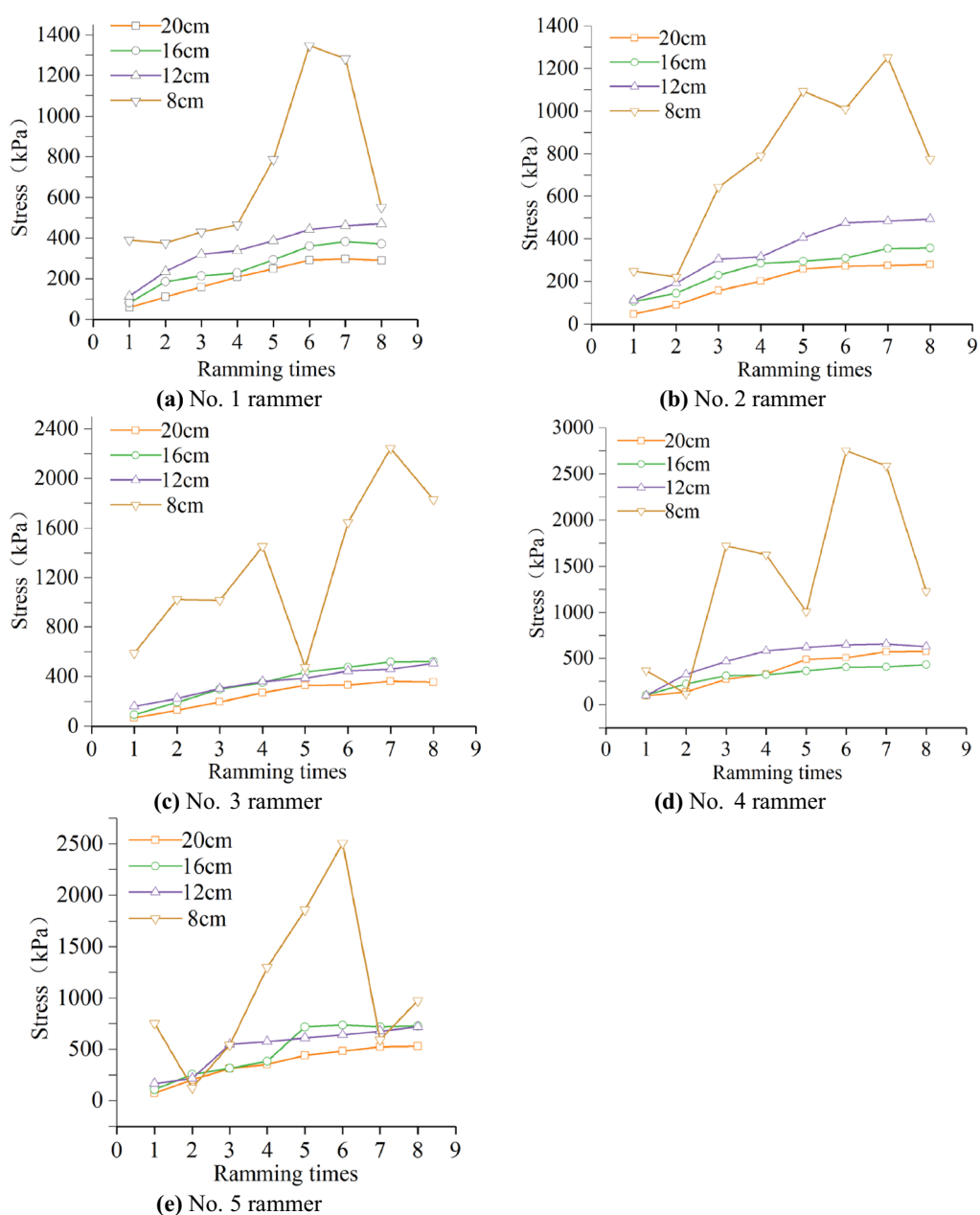


**Fig. 11** Stress characteristics of different soil-laying thickness and ramming times (experiments)

and 20 cm, the received ramming stress decreases. When the paving thickness is 20 cm, the ramming energy received by the No. 1 and No. 2 rammers is less than 300 kPa. When the paving thickness is 16 cm, the ramming energy received by the No. 1 and No. 2 rammers is less than 450 kPa. The maximum ramming energy is above 300 kPa subject to the action of other paving thicknesses and different rammers.

#### Analysis of single-layer ramming stress characteristics

To gain insight into the mechanism and structural characteristics of the traditional ramming technology, the trend of the ramming stress during the process of ramming, and the transmission law and influence rule of the stress wave in the laminated layer are monitored by measuring the ramming stress. The recovery coefficient

of different ramming times and the action mechanism of the ramming stress field of the ramming hammer are discussed in detail based on dynamics and elastoplastic theory to reveal the action mechanism and scientific connotation of the traditional tamping technology.

### Obtaining numerical simulation parameters

To simulate the real ramming situation, the mechanical properties of the rammed soil layer were evaluated by changing the internal friction angle and cohesion of the rammed soil to the mechanical properties of the soil at various ramming cycles. In the numerical simulation, the No. 2 rammer was selected, the thickness of the layer was 12 cm, and the effects corresponding to eight ramming times were achieved. The mechanical properties of the soil were obtained according to triaxial tests.

The triaxial tests's cylindrical sample (three samples in all) had radii equal to 50 mm and heights equal to 100 mm, and moisture contents of 13.8% and densities of 1.65 g/cm<sup>3</sup> were achieved. The static triaxial test was conducted using a Global Digital Systems Instruments (GDS) unsaturated triaxial apparatus to measure the constitutive relationship of the rammed soil materials used in this test. The tests were conducted at the confining pressures  $\sigma_3$  of 50 kPa, 100 kPa, 150 kPa, and 200 kPa. The values of  $\sigma_1$  were measured to be 190.95 kPa, 307.71 kPa, 358.74 kPa, and 506.76 kPa, respectively. According to the requirements, the test values can be analyzed with the Mohr circle diagram (Fig. 12), and the cohesive force of the soil sample in this state was 25.14 kPa, the friction angle was 30.23°.

According to the stress–strain curve (Fig. 13) of the sample at different confining pressures  $\sigma_3$  during the test, the section with a better elastic state was eliminated from the resulting curve, and its elastic modulus after fittings were 11.05, 15.74, 17.30, and 20.66 MPa, respectively. The average value was 16.19 MPa. Table 6 shows the parameters of soil samples used in the simulation.

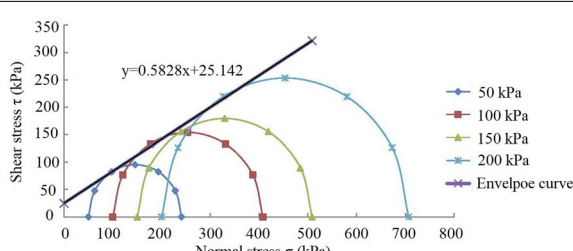


Fig. 12 Mohr circle

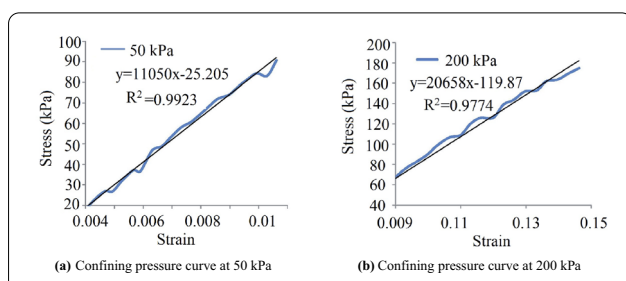


Fig. 13 Stress–strain curves

### Modeling and analysis of mechanism

The finite element software ABAQUS (version 2016, Dassault Systems) was used for simulations. To reduce the number of calculations, the rammer was set as a rigid body, and the rammer and covering soil model was simplified to a planar two-dimensional model. According to axisymmetric conditions, 1/2 rammer and covering soil were used for modeling. The finite element modeling adopted the linear reduction integral unit CAX4R, the total number of units of the rammer were 66 and 82 nodes (along the Y and X direction, respectively), and the total number of units that covered the soil were 2400 and 2525 nodes (along the Y and X directions respectively). Analysis of the stone pestle unearthed from the No. 3 mausoleum (Western Xia Imperial Tombs) indicated that its weight was 3.34 kg, its diameter was 14.17 cm, its height was 14.54 cm, its volume was 1632.51 cm<sup>3</sup>, its density was 2.047 g/cm<sup>3</sup>, and the material was sandstone. According to its curvature and diameter, a hemispherical rammer with a diameter of 12 cm and a mass of 4.03 kg was used for simulation. The height of the falling distance was 0.25 m, the thickness of the covering soil was 12 cm, while the specific simulation model is shown in Fig. 14.

### Basic assumptions

1. The rammed soil layer was homogeneous, continuous, and isotropic,
2. the soil was regarded as a semi-infinite space in the horizontal direction,
3. the rammer itself did not rotate,
4. the rammer was in free fall Fig. 15.

### Theoretical calculation and analysis

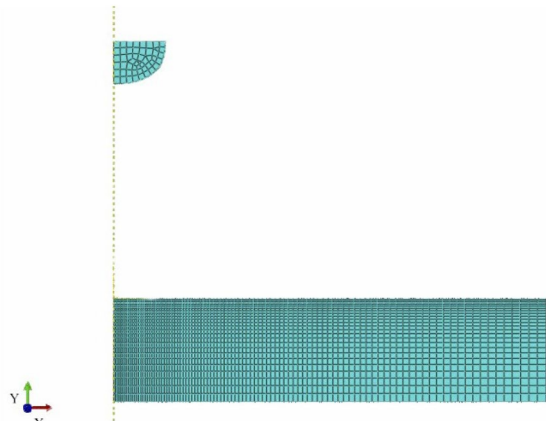
Hertz studied the maximum impact force of two elastic spheres with masses equal to  $m_1$  and  $m_2$  when these collided at speed  $v$ , and expressed it with the following equation [28]:

$$F_m = k^{2/5} \left[ \frac{5}{4} v^2 \frac{m_1 m_2}{m_1 + m_2} \right]^{3/5} \quad (4)$$

where  $k$  is given by the following equation:

**Table 6** Soil sample parameters used in simulations

Types	Young's modulus (MPa)	Poisson's ratio	Internal friction angle (°)	Cohesion (kPa)	Dilatancy angle (°)	Density (g/cm <sup>3</sup> )
Test soil	16.19	0.3	30.23	15–30	10.17	1.65

**Fig. 14** Dynamic simulation model of rammed earth

$$k = \frac{4}{3\pi} \sqrt{\frac{r_1 r_2}{r_1 + r_2}} \frac{1}{C_1 + C_2} \quad (5)$$

$$C_1 = \frac{1 - \mu_1^2}{\pi E_1} \quad C_2 = \frac{1 - \mu_2^2}{\pi E_2} \quad (6)$$

where  $r_1$  and  $r_2$  are the radii of the two spheres,  $E_1$  and  $E_2$  are the elastic moduli of the two spheres, and  $\mu_1$  and  $\mu_2$  are the Poisson's ratios of the two spheres. When the rammer impacted the foundation, the rammer was not necessarily a sphere and the foundation soil was not an elastomer, but some qualitative analysis can be made by using Hertz's collision theory. The deformation modulus  $E_1$  of the No. 1 rammer was much larger than the deformation modulus  $E_2$  of the foundation soil, i.e.,  $E_1 = \infty$ . The foundation soil can be regarded as a half-space elastic deformation body, thus,  $r_2 = \infty$ , and  $m_2 = \infty$ . In

addition, we set  $m_1 = M$ ,  $E_2 = E_s$ ,  $r_1 = R$ , and  $\mu_2 = \mu$ . Therefore, Eq. (3) becomes

$$C_1 = 0 \quad C_2 = \frac{1 - \mu^2}{\pi E_s} \quad (7)$$

In Eq. (7),  $E_s$  and  $\mu$  are the deformation modulus and Poisson's ratio of the foundation soil, respectively. Thus, Eq. (2) can be changed to,

$$k = \frac{4}{3} R^{\frac{1}{2}} \frac{E_s}{1 - \mu^2} \quad (8)$$

In Eq. (5),  $R$  is the radius of the rammer. If Eq. (5) is substituted in Eq. (1) and  $v^2 = 2gh$  is considered, then Eq. (1) can be simplified to

$$F_m = 1.944 R^{\frac{1}{2}} m^{\frac{3}{4}} \left[ \frac{E_s}{1 - \mu^2} \right]^{\frac{2}{5}} (gh)^{\frac{3}{5}} \quad (9)$$

In the experiment, the contact area between the rammer and the paving layer was equivalent to the projected area  $S$  of the surface where the diameter of the shaped rammed nest was located. Thus, the maximum impact stress of the rammer was

$$\sigma_m = \frac{F_m}{S} \quad (10)$$

Based on measurements, we found that the projected area of the ramming pit was mainly affected by the weight of the rammer, while the influence of the soil-paving thickness on the projected area could be ignored. This is owing to the different potential energies generated by different rammers subject to the same condition, that is to say, the impact energies on the paving soil were different. The specific expression is as follows,

$$S = \pi R^2 \left\{ \begin{array}{l} \left( 0.13 + 0.2 \sin(0.5\pi dN) + 0.9e^{-0.16N^2} \right) \left( \frac{m_0}{m} \right)^{\frac{1}{2}} \left( \frac{d}{0.12} \right)^{\frac{3}{10}} \\ 0.24 + 6 \sin(-0.0004\pi dN) + 0.6e^{-0.09N^2} \left( \frac{d}{0.2} \right)^{\frac{3}{10}} \end{array} \right. \quad (11)$$

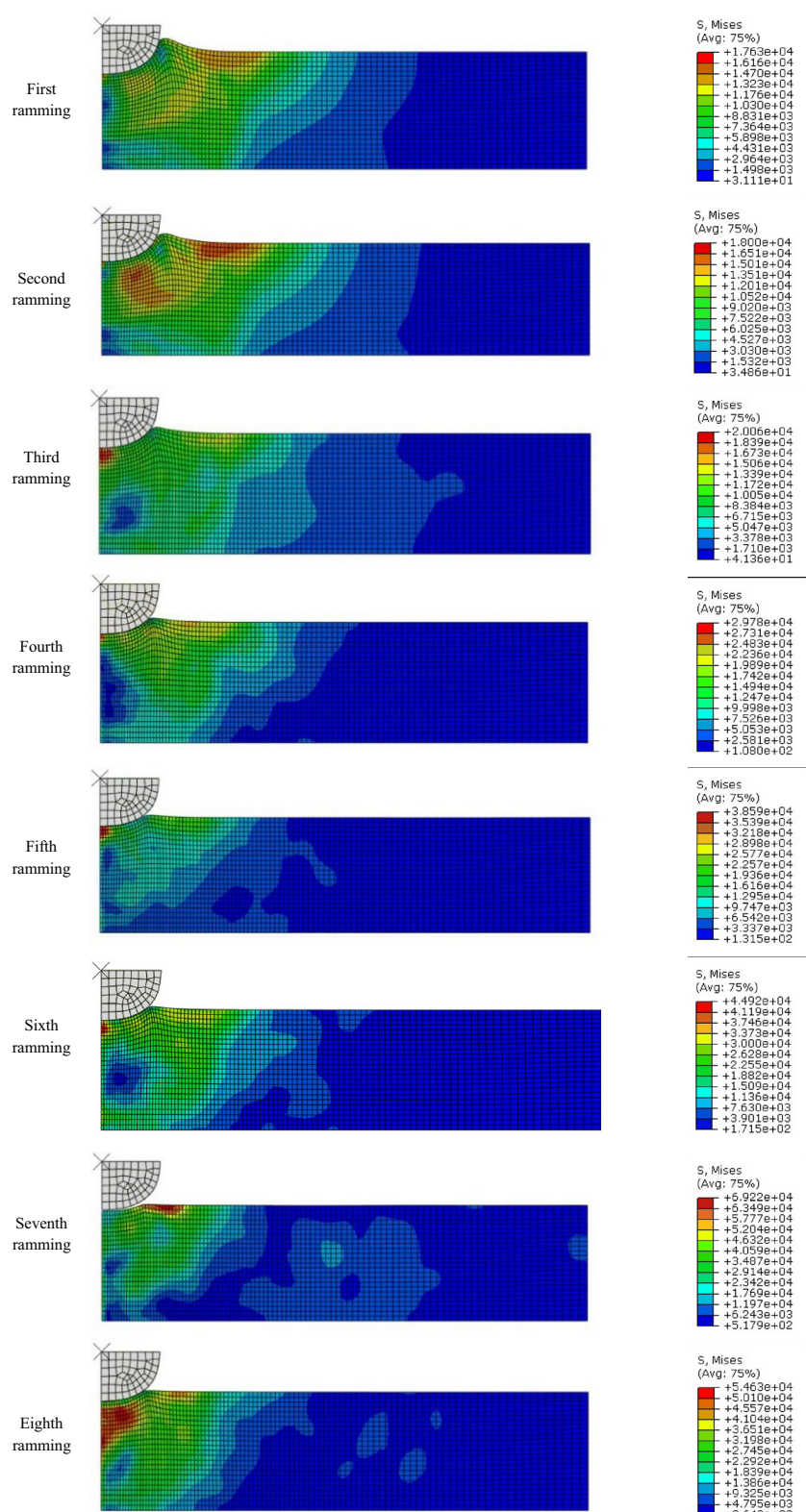


**Fig. 15** Pavement stress nephograms of rammer at different ramming times

The problem of collision between the rammer and foundation soil is different from that of the general elastomer and elastoplastic body because there are not only elastic and plastic deformations, but also viscosity, hardening, and friction energy dissipation in the collision process between the rammer and the foundation soil [29–31]. The maximum impact stress of the rammer must be reduced owing to the collision characteristics described above. According to the analysis of the calculation method of impact stress Eqs. (3–11), it is concluded that different rammer diameters (weight, cross-sectional area) and layer thicknesses mainly affect the internal friction angle and cohesion of the buffer layer. Therefore, the maximum impact stress must be corrected, and a parameter influence coefficient  $\lambda$  is derived. The actual maximum impact stress value is obtained by multiplying the calculated result of the elastoplastic Hertz contact theory by a parameter  $\lambda$  (parameter influence coefficient). The calculation formula is as follows

$$\sigma = \lambda \sigma_m \quad (12)$$

The parameter influence coefficient  $\lambda$  was calculated according to the experimental data subject to the working condition of rammer No. 1 and a paving soil thickness equal to 12 cm. Polynomial fitting was conducted with the use of the calculated parameter influence coefficient as follows,

$$\lambda = \begin{cases} \frac{a}{3 + e^{0.1N}} & 2R > d \cap m \leq 3m_0 \\ \frac{a}{1 + e^{0.2N}} & \text{others} \end{cases} \quad (13)$$

and

$$a = \begin{cases} 0.3 \left( \frac{mH}{m_0 d} \right)^{\frac{4}{5}} N^{\frac{13}{10}} \left( 0.1 + 0.2 \sin \left( \frac{dN\pi}{2} \right) + e^{-0.16N^2} \right) & 2R \leq d \cap m \leq 3m_0 \\ 0.25 \frac{m}{m_0} N^{\frac{1}{2}} \frac{H}{d} & 2R > d \cap m < 3m_0 \\ 0.2 \left( \frac{m}{m_0} \right)^{\frac{2}{5}} N^{\frac{4}{5}} \left( \frac{H}{d} \right)^{\frac{1}{2}} & \text{others} \end{cases} \quad (14)$$

where  $m_0$  is the minimum weight of the rammer subject to this working condition and is equal to 3.32 kg,  $H$  is the drop height of the rammer,  $d$  is the thickness of the paving soil, and  $m$  is the weight of the rammer. Additionally,  $a$  is the dimensionless coefficient, and the correction factor  $\lambda$  is the dimensionless parameter. Fig. 16 shows the effect of soil thickness and rammer quality on parameter  $a$ . In the figure,  $X_1$  represents the paving thickness,  $X_2$  represents the rammer mass, and  $Y$  represents parameter

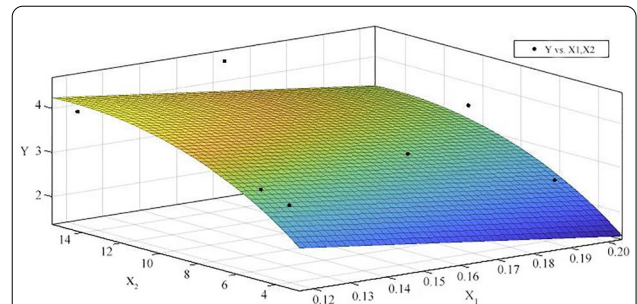


**Fig. 16** Influence of thickness of paving soil and weight of rammer on parameter  $a$

a. When the rammer weight increases,  $a$  increases; when the paving thickness increases,  $a$  decreases.

Comparison of the theoretical calculation value and the actual value obtained from Eqs. (13) and (14), and the fitting curve in Fig. 17, it can be concluded that the overall trend of different working conditions is that the error decreases gradually as a function of the ramming times. This is attributed to the fact that as the number of ramming times increases, the layer density and elastic modulus increase, while as the transmission energy consumption of the impact wave decreases, the detection accuracy of the sensor increases, and the theoretical calculation value becomes closer to the actual contact force. Based on the test results, we found that when the thickness of the paving soil was 20 cm, the consolidation and stratification of the paving soil layer would occur after ramming with the No. 1 and No. 2 rammers. This means that there is no uniform compaction within the range of the paving soil thickness. It has been proved that the ramming energies of the No. 1 and No. 2 rammers

were not sufficient to be transmitted to the bottom part of the rammed layer, or the energy transmitted to the bottom part was too small to be rammed. To achieve the ideal rammed state, the ramming energy of the rammer should be increased and analyzed according to actual operation and measured data. When the No. 1 and No. 2 rammers rammed the layer that had a thickness of 20 cm, the measured impact stress was less than 300 kPa. Therefore, when the thickness of the rammed layer is fixed, the

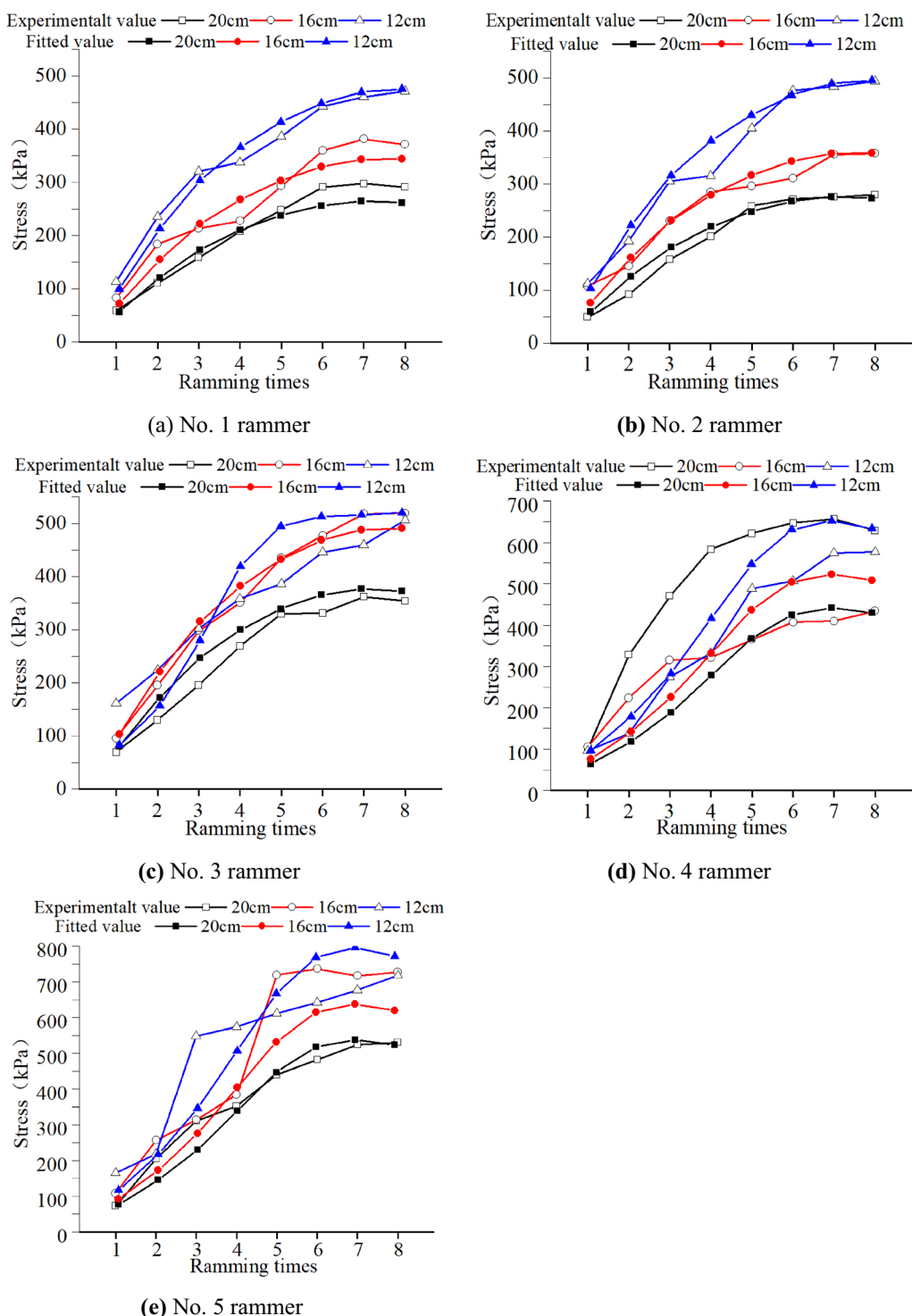


**Fig. 17** Coupling relationship between experimental value and fitted value of different rammers and ramming times

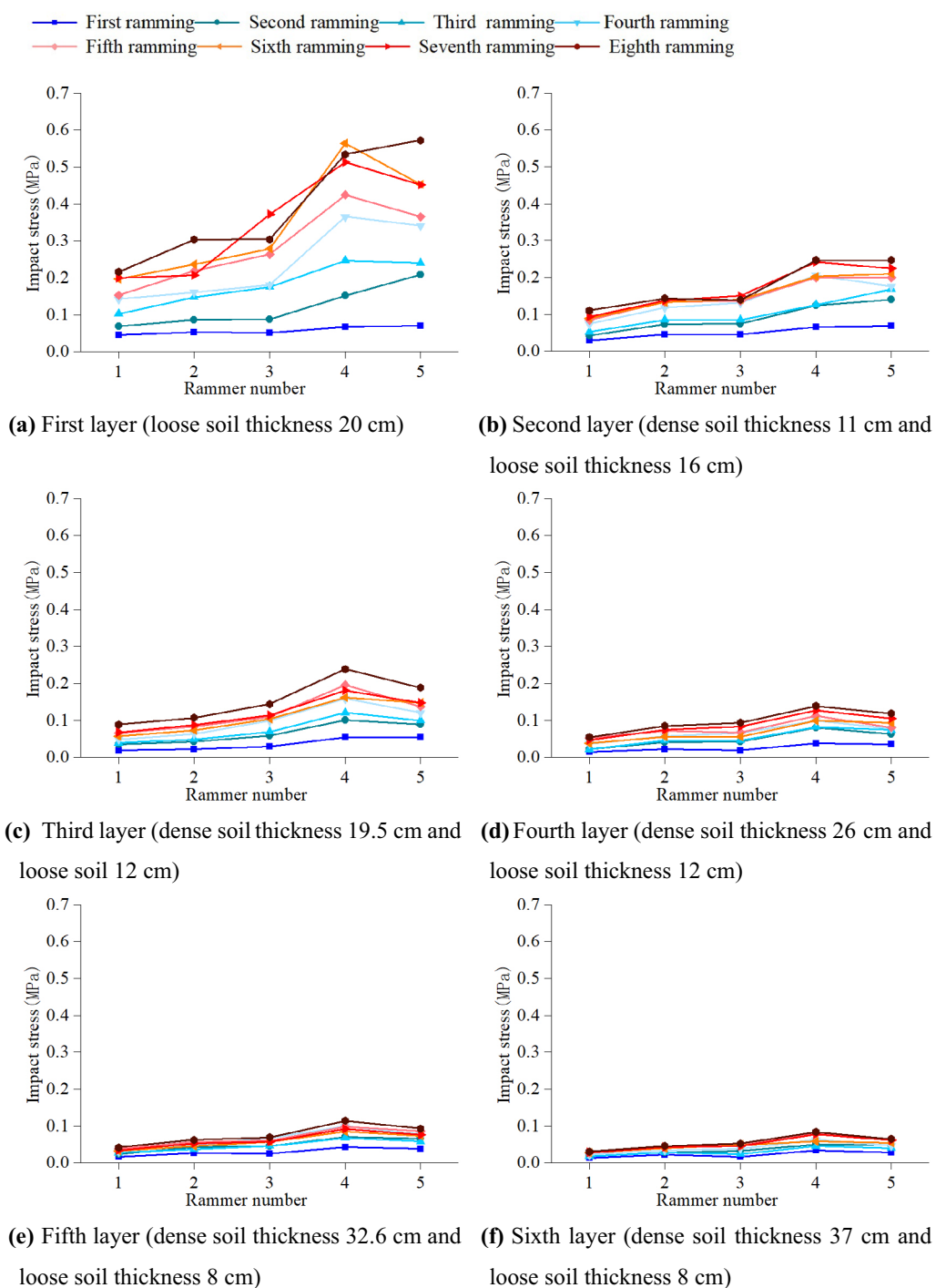


**Fig. 18** Impact stress of pressure box when ramming layer is increased(experiments)

actual impact stress value can be calculated with Eqs. 13 and 14. The deviation of the data of some paving thickness was large that was mainly owing to the influences of

the soil particles, ramming technology, and other aspects in the test process, showing that the adaptability of the rammer used was not high and the error was large.

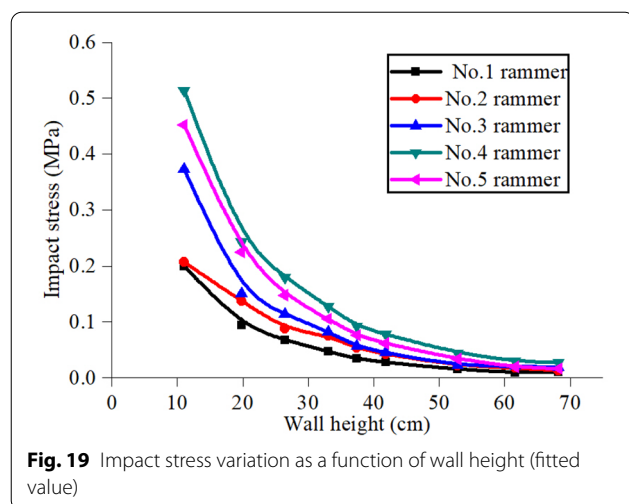


**Fig. 19** Impact stress variation as a function of wall height (fitted value)

### Analysis of multi-layer ramming stress characteristics

The energy generated by the rammer is transmitted in the form of vibration. The wave of the ramming mainly propagates vertically in the downward direction and horizontally. To understand the ramming stress response, the first layer can be perceived as the ramming layer that increases during the tamping process. Accordingly, the first, second, third, fourth, fifth, and sixth layers were paved at 20 cm, 16 cm, 12 cm, 12 cm, 8 cm, and 8 cm, respectively, to test the ramming stress. The transmission characteristics and influence range of the tamping energy were divided in all directions.

#### Analysis of vertical tamping stress characteristics

As it can be observed from Fig. 18, when the thickness of the paving soil is 20 cm, the single-layer ramming stresses experienced by rammers No. 1 to No. 5 were basically the same during the first and second ramming cycles. In the process of ramming from 3 to 8 times, the increase in the ramming stress of rammers 3–5 was large, and that of hammers 1–2 was small. With the gradual increase of the ramming layer, the ramming stress experienced by the bottom layers (stratum) gradually decreased. When the thickness exceeded 40 cm

(6th layer), the stress received by the bottom layers from all the rammers was almost zero. When the thickness exceeded 30 cm (4th layer), the stress experienced by the bottom layers of the No. 1 to No. 3 rammers was very small.

The scientific basis of the traditional ramming technology was based on the fact that the stratum was denser when an infinite number of superposition ramming times were executed. As the ramming height increases, the soil of the lower layer is compacted and consolidated in the process of ramming the upper layer. At the same time, the higher the quality of the rammer, the stronger the ramming energy received by the lower layer. This is another prominent feature of higher-level soil building walls that are often rammed with higher quality rammers.

For rammers No. 1 to No. 5, the impact stress experienced by the second layer after the first layer was paved, and ramming was reduced to 46%, 53%, 53.2%, 53.8%, and 50%. After the two layers were rammed following an increase in the ramming energy, the impact stress of the pressure box first increased and then decreased. The reduction of rammer 3 was the largest. During the ramming process, when the thickness reached 39.6 cm, the impact stresses of rammers No. 1 to No. 5 were 0.0308 MPa, 0.0456 MPa, 0.05275 MPa, 0.084 MPa, and 0.0646 MPa, and the impact stress of the No. 4 rammer was the largest. This phenomenon shows that subject to the action of the No. 1–5 rammers, increases in the ramming height, the deceleration rate of impact stress first increased and then slowed down. As the ramming energy increased, the reinforcement depth also increased. However, the reinforcement depth was also affected by other factors. Rammers No. 1–5 basically converged to 68.2 cm, and the attenuation of ramming stress was almost zero.

As it can be observed from Fig. 19, the ramming stress attenuation can be divided into three stages. Wall heights between 10 and 20 cm were considered to be the first stage. In this stage, the slope of the curve was the largest, and the response was approximately linear. This was more prominent for rammers No. 3 to No. 5 than No. 1 to No. 2. Wall heights in the range of 20–40 cm were the

**Table 7** Fitting equation of impact stress of multiple layers with different rammers

Rammer	Fitting equation	Correlation coefficient $R^2$	Area expression	Curve integral area ( $m^2$ )
No. 1	$y = 0.00573 + 0.39464e^{-x/14.3695}$	0.99151	$y = -5.696e^{(-x/14.3695)} + 0.00573x + C^1$	0.22
No. 2	$y = -0.002 + 0.34425e^{-x/21.0534}$	0.99448	$y = -7.2476e^{(-x/21.0534)} - 0.002x + C^2$	0.19
No. 3	$y = 0.001,534 + 0.8721e^{-x/11.83216}$	0.98771	$y = -10.3188e^{(-x/11.8322)} + 0.001534x + C^3$	0.48
No. 4	$y = 0.00906 + 0.95481e^{-x/15.58366}$	0.9875	$y = -14.8794e^{(-x/15.5837)} + 0.00906x + C^4$	0.54
No. 5	$y = -0.00309 + 0.83206e^{-x/16.28111}$	0.9896	$y = -13.5469e^{(-x/16.2811)} - 0.0031x + C^5$	0.46

second stage, and the curve slope was obviously reduced. This effect was more obvious for rammers No. 3 to No. 5 than rammers No. 1 or No. 2. The third stage involved wall heights in the range of 40–70 cm. At this stage, in comparison with the other two stages, the curve slope was the smallest and the attenuation rates for rammers No. 1–5 were almost the same. The correlation coefficient for fitting the convergence equation of the impact stress of different rammers was higher than 0.98.

On this basis, the area integral of the curve is estimated within the interval of [11, 68.2], and the area integral expression is,

$$A = \int_{x_1}^{x_2} f(x) dx = [F(x)]_{x_1}^{x_2} = [Ae^{-x/B} + Dx + C^*]_{x_1}^{x_2} \quad (15)$$

A, B, and D are constants, and their values for different types of rammers are listed in Table 7. The value of the constant  $C^*$  is determined by the following formula,

$$C^* = \begin{cases} -\left(Ae^{-x/B} + Dx\right), & [0, 11] \cup [68.2, \infty) \\ 0, & (11, 68.2) \end{cases} \quad (16)$$

The fitting curve equation, integral equation, and integral area are listed in Table 7.

(2) Characteristic distribution of tamping stress in horizontal direction.

It was found that with the increase of ramming layers, the overall ramming stress increased as a function of the ramming times, and the horizontal displacement of soil was distributed symmetrically. With an increase in the horizontal distance and depth from the ramming point, the horizontal displacement gradually decreased.

As it can be observed in Figs. 20 and 21, the impact ranges of the rammers No. 1 to No. 5 extend as far as 72 cm, and the effective range of ramming stress is not more than 48 cm. With the increase in ramming times, the increase in ramming stress is more obvious. This is related to the propagation of the compression wave after compaction. As the ramming density tended to stabilize, the ramming stress hardly increased, and the obvious impact range was less than 24 cm. The ramming stresses of the No. 1 rammer in the first to fourth layers were 250 kPa, 100 kPa, 75 kPa, and 50 kPa. The ramming stresses of the No. 2 rammer in the first to sixth layers were 325 kPa, 175 kPa, 150 kPa, 100 kPa, 75 kPa, and 50 kPa. The ramming stresses of rammer No. 3 in the first to sixth layers were 400 kPa, 175 kPa, 150 kPa, 100 kPa, 75 kPa, and 50 kPa. The ramming stresses of rammer No. 4 in the first to sixth layers were 750 kPa, 300 kPa, 175 kPa, 150 kPa, 100 kPa, and 80 kPa. The ramming stresses of rammer No. 5 in the first to sixth layers were 650 kPa, 250 kPa, 180 kPa, 120 kPa, 100 kPa, and 75 kPa.

It can be inferred that as the weight of the rammer increased, the attenuation of the ramming stress became faster. After the fourth layer, the ramming stresses of rammers No. 1 to No. 5 were almost similar. As the ramming layer number increased, the ramming stress attenuation in the vertical direction was very rapid. When the height increased to 35 cm (fourth layer), the ramming stresses of the rammers No. 1 to No. 5 were less than 100 kPa. In addition, the minimum diameter of the rammer was 10 cm, and the diameter of the No. 5 rammer was 18 cm. This means that the ramming stress decayed rapidly to zero within a spatial range that was less than 3 cm on both sides of the rammer.

## Conclusion

Based on field tests of a single layer with different rammers, soil thickness, and times of ramming and multi-layer stacked ramming, the following conclusions were made:

(1) In the process of single-layer ramming, the ramming stress of the rammed earth could be divided into three stages with the increase of ramming times. The first stage ranged from the first to the sixth ramming times. During this process, the ramming energy increased rapidly the increase of ramming times, the plastic deformation decreased gradually, the energy was mainly consumed by ramming vibration, the elastic modulus increased gradually, and a plastic constitutive model was considered. The second stage was from the 6th to the 8th ramming times. The ramming energy converged slowly, the plastic deformation area was stable, and the rammed earth was an elastoplastic transition constitutive model. The third stage occurred when the ramming times were more than eight times. The ramming energy was stable, and the rammed earth was in an elastic vibration state.

(2) The traditional compaction process conforms to the Hertz contact theory of elasticity and plasticity. Based on the measured stress of the alternating variation of the three variables of the weight of the rammer, the thickness of the paving soil, and the number of ramming, this paper puts forward the calculation method of the impact stress of the rammer. It is estimated that this method is in line with the quality assessment of the second stage. When the measured impact stress is less than 300 kPa, the tamping effect is not obvious.

(3) Based on calculations, it was found that the depth of the continuous work expended by the rammer to the lower layer was not more than 68.2 cm (six layers of ramming), the ramming stress decayed

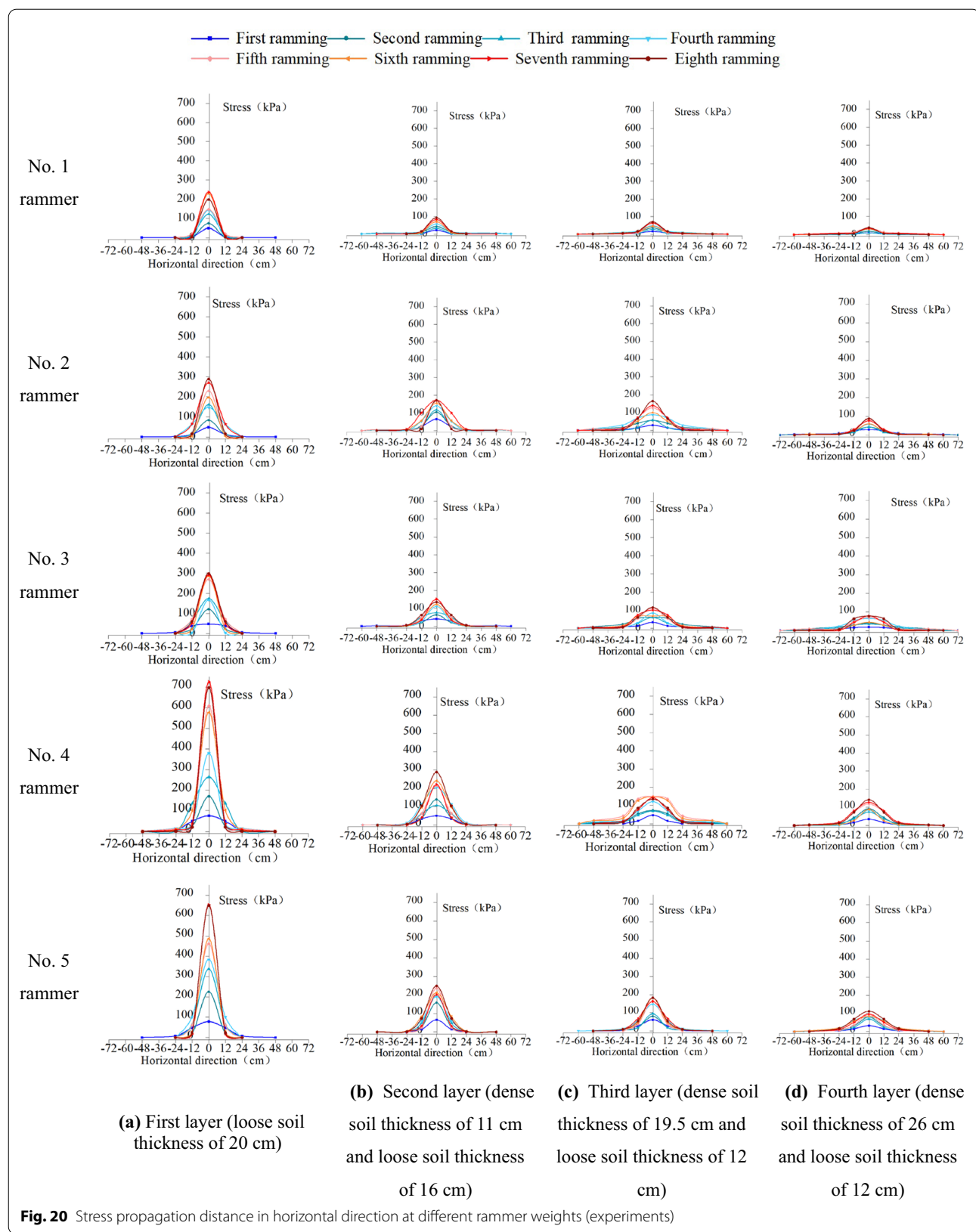
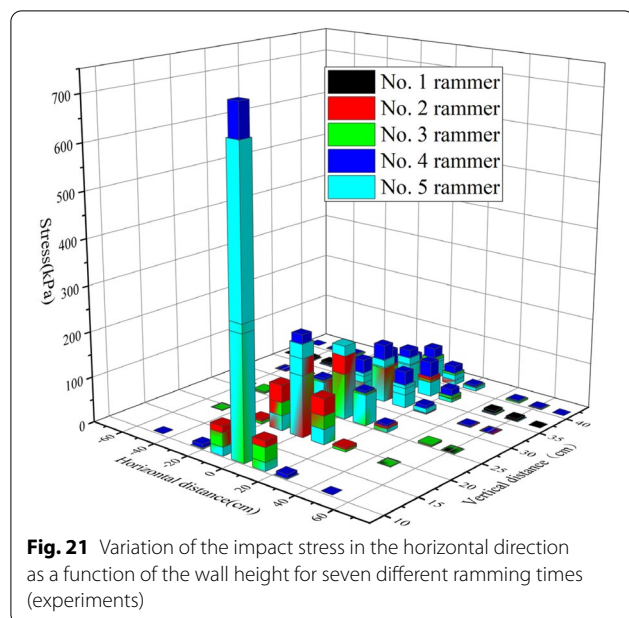


**Fig. 20** Stress propagation distance in horizontal direction at different rammer weights (experiments)



rapidly as a function of the ramming layer, and the attenuation rate decreased exponentially in turn. The ramming stress was less than 100 kPa when the ramming layers increased to six in the vertical direction, and it decayed to 50 kPa when the tamping layers increased to four in the horizontal direction.

(4) To energy dissipation, the depth and width of reinforcement were different for different weights of rammers. As the weight of rammers increased, the depth and width of the impact stress increased proportionally, and the attenuation speed of the ramming stress in the horizontal direction increased compared with that in the vertical direction. In terms of the diffusion distance of the tamping stress in the horizontal direction, the width of the impact stress of different rammers is almost the same (the diffusion to both sides is less than 3 cm), and the distribution is symmetrical. The contribution of ramming to the reinforcement in the horizontal direction is limited. During the ramming process, the reverse upwelling impact force along the horizontal direction and the unevenness of ramming layer were effectively compensated by the traditional process of overlapping ramming based on "chong hai wo, hang yin ding."

(5) Based on the impulse theorem, combined with the actual ramming process and the mathematical calculation method of finite element analysis, the fitting formula of ramming stress has a high degree of consistency with the measured ramming data.

This model is an innovative attempt to transfer the ancient ramming technique to the scientific quantification process in the field of earthen sites conservation. In view of the validity and applicability of the mathematical model calculation method in this paper, it can provide reference for the scientific cognition of other aspects of construction technique of earthen sites.

(6) The limitation of this study is that the idealized assumptions in the modeling process can not fully reflect the actual situation of the earthen site, such as the anisotropic characteristics of the actual soil and the interference of human factors, and the ramming mechanical model proposed in this paper for a single compacted soil is another aspect of its limitations. According to the above limitations, starting from the complex environment of ramming technique of earthen sites, the direction for the future research on the accurate modification and universal applicability of the mathematical model of compaction mechanism is pointed out.

#### Acknowledgements

Not applicable.

#### Author contributions

Conceptualization, QP and QG; data curation, ZH and XL; formal analysis, QP and XL; funding acquisition, QG and QP; investigation, GZ; writing—original draft, BZ; writing—review & editing, QG. All authors read and approved the final manuscript.

#### Funding

This work was financially supported by the National Key R&D Program of China "Research on structural instability mechanism and control technology of earthen sites under static and dynamic loads" (2020YFC1522203), Talent Training and Introduction Program of CAS "Light of the West", Supported by Natural Science Foundation of Gansu Province, "On Dynamic Response Characteristics of Earthen Sites Reinforced by Ramming and Propping" (Grant number 21JR7RA757).

#### Availability of data and materials

Not applicable.

#### Declarations

##### Competing interests

Not applicable.

##### Author details

<sup>1</sup>Dunhuang Academy, Mogao Grottoes, Dunhuang 736200, Gansu, China.

<sup>2</sup>Key Laboratory of Mechanics On Disaster and Environment in Western China of Ministry of Education, Lanzhou University, Lanzhou 730000, Gansu, China.

<sup>3</sup>National Research Center for Conservation of Ancient Wall Paintings, Dunhuang 736200, Gansu, China. <sup>4</sup>Cultural Heritage Conservation and Design Consulting Co, Ltd of Mogao Grottoes, Dunhuang 736200, Gansu, China. <sup>5</sup>College of Culture Heritage, Northwest University, Xi'an 710069, China.

Received: 27 May 2022 Accepted: 14 August 2022

Published online: 01 September 2022

## References

1. Cromley E. Cultural embeddedness in vernacular architecture. *Build Res Inf*. 2008;36:301–4. <https://doi.org/10.1080/09613210801902995>.
2. Yuan GK, Hou Y. Looking at the relative age of the early Shang city sites from the ramming technology of the city walls. *Cultural Relic*. 2007;12:75–8 (in Chinese).
3. Du Y, Chen W, Cui K, et al. Study on the linear absent section ratio (L-ASR) of earthen sites and anthropogenic influence from the perspective of population density. *Herit Sci*. 2021. <https://doi.org/10.1186/s40494-021-00582-5>.
4. Ngowi AB. Improving the traditional earth construction: a case study of Botswana. *Constr Build Mater*. 1997;11(1):1–7. [https://doi.org/10.1016/S0950-0618\(97\)00006-8](https://doi.org/10.1016/S0950-0618(97)00006-8).
5. Zhang QJ, Chen WW, Yuan PB. Experimental study on impregnation and consolidation effects of modified polyvinyl alcohol solution for coarse-grained soils: a case study on the Subashi Buddhist Temple Ruins of China. *Bull Eng Geol Env*. 2020;79(3):1487–500. <https://doi.org/10.1007/s10064-019-01622-y>.
6. Attia DA, Maarouf I, Taha D, Nassar D. Detecting failures in conservation practice in relation to cultural significance: the case of heritage buildings in Khartoum. *Build Res Inf*. 2020;48(1/2):124–39. <https://doi.org/10.1080/09613218.2019.1654842>.
7. Pei QQ, Chen JR, Wu HC, et al. A preliminary study on the principles for building foundations, cities and walls in Yingzao Fashi. *Dunhuang Res*. 2021;189(5):145–58 (in Chinese).
8. Zhang HJ. A brief study on ancient Punner. *J Henan Univ Sci Technol*. 2006;5:17–20 (in Chinese).
9. Wang XZ. Shallow discussion on accuracy control of large-span steel box girder hoisting. *Shanxi Archit*. 2011;37(18):85–7 (in Chinese).
10. Silva RA, Jaquin P, Oliveira DV, et al. Conservation and new construction solutions in rammed earth. *Struct Rehabilit Old Build*. 2014;2:77–108. [https://doi.org/10.1007/978-3-642-39686-1\\_3](https://doi.org/10.1007/978-3-642-39686-1_3).
11. Xue C, Xu Y. Study on ramming technique of the Beacon tower in Xinjiang—Taking Kizilgaha Beacon tower as an example. *Herit Conserv Stud*. 2017;2(07):70–2 (in Chinese).
12. Fu J, Zhang N. A study on the construction technology of the Qin Shi Huang's Mausoleum. *Wen Bo*. 2014;181(04):35–8 (in Chinese).
13. Xia W. Performance and construction of raw soil materials based on ramming technology. *Shaanxi Educ*. 2019;9:20–1 (in Chinese).
14. Li B. Rediscovering rammed earth. *Time. Architecture*. 2014;3:66–71. <https://doi.org/10.3969/j.issn.1005-684X.2014.03.012>.
15. Zhou TG, Peng DQ, Jun Mu, et al. Research and application of modern rammed earthwall construction technology. *Constr Technol*. 2012;41(15):39–42 (in Chinese).
16. Zhang B, Wang XD, Guo QL, et al. Quality control research on reinforcement technology tests using rammed earth to fill unsupported walls in a western Xia Imperial Tomb. *Dunhuang Res*. 2016;159(05):135–41 (in Chinese).
17. Pei QQ, Zhang B, Liu XY, et al. Research on the rammed quality and influencing factors of traditional rammed technology. *Chin J Rock Mech Eng*. 2020;39(S2):3557–69 (in Chinese).
18. Kianfar E, Toufighi V. Reliability analysis of rammed earth structures. *Constr Build Mater*. 2016;127:884–95. <https://doi.org/10.1016/j.conbuildmat.2016.10.052>.
19. Ciancio D, Jaquin P, Walker P. Advances on the assessment of soil suitability for rammed earth. *Constr Build Mater*. 2013;42:40–7. <https://doi.org/10.1016/j.conbuildmat.2012.12.049>.
20. Pei Q. Scientific cognition and stability evaluation of traditional technology for rammed earthen heritage sites. PhD thesis, Lanzhou University. 2020. (in Chinese).
21. Yuan J. A ten-year review of the Chinese civilization origination project: research on technology and production in the origin and early development of Chinese civilization. *South Herit*. 2012;4:11–8 (in Chinese).
22. Loccarini F, Ranocchiai G, Rotunno T. Experimental and numerical analyses of strengthened rammed earth masonry arches. *Comput Struct*. 2020. <https://doi.org/10.1016/j.compstruc.2020.106329>.
23. Aubry D. Computational soil dynamics and soil-structure interaction. *Dev Dyn Soil Struct Interact*. 1993;390:43–60. [https://doi.org/10.1007/978-94-011-1755-5\\_3](https://doi.org/10.1007/978-94-011-1755-5_3).
24. Chang D, Lai Y, Yu F. An elastoplastic constitutive model for frozen saline coarse sandy soil undergoing particle breakage. *Acta Geotech*. 2019;14:1757–83. <https://doi.org/10.1007/s11440-019-00775-0>.
25. Liu Jh, Jb Yuan, Xiong H, et al. Dynamic compaction treatment technology research of red clay soil embankment in southern mountains. *J Cent South Univ Technol*. 2008;15:50–7. <https://doi.org/10.1007/s11771-008-0435-7>.
26. Qiu JJ, Liu MC, Guo YT. On the use of the tamping energy in dynamic compaction of the foundation with large fill depth. *Rock Soil Mech*. 1995;4:57–65. <https://doi.org/10.16285/rsm.1995.04.008>.
27. Yang JY, Pen ZZ. Research on reinforcement model and range of tamping energy in red sandstone soil. *J Jiangxi Univ Sci Technol*. 2015;000(001):37–42 (in Chinese).
28. Bai B. Research on the impact force of rammer. *Chin J Undergr Space Eng*. 2020;02:92–5 (in Chinese).
29. Tian S, Wang Z. Effect of impact mode on treatment effect of dynamic compaction. *Rock and Soil Mechan*. 2008;29(11):3119–23. <https://doi.org/10.3724/SPJ.1005.2008.00527>.
30. Liu X. Affection of tamping energy and tamping times depth of dynamic consolidation. PhD thesis, Central South University. 2008. (in Chinese)
31. Duan W. The method of determining the optimal number and research about evaluation of effective energy of dynamic compaction. M thesis, North Central University. 2016. (in Chinese)

## Publisher's Note

Springer Nature remains neutral with regard to jurisdictional claims in published maps and institutional affiliations.

Submit your manuscript to a SpringerOpen® journal and benefit from:

- Convenient online submission
- Rigorous peer review
- Open access: articles freely available online
- High visibility within the field
- Retaining the copyright to your article

Submit your next manuscript at ► [springeropen.com](http://springeropen.com)